Materials Horizons

ROYAL SOCIETY OF CHEMISTRY

COMMUNICATION

View Article Online
View Journal | View Issue

Check for updates

Cite this: *Mater. Horiz.*, 2025, **12**, 1290

Received 27th August 2024,
Accepted 20th November 2024

DOI: 10.1039/d4mh01153h

rsc.li/materials-horizons

Incarcerating bismuth nanoparticles into a thiol-laced metal–organic framework for electro and photocatalysis†

Parijat Borah, ‡*[a] Natalie McLeod, ‡[ab] Nipun Kumar Gupta, [a] Reuben J. Yeo,[a] Tanmay Ghosh, [a] Zainul Aabdin, [a] Lidao Li,[a] Prajna Bhatt, [b] Yuhan Liu, [b] Robert Palgrave, [b] Yee-Fun Lim, [c] Zhengtao Xu *[a] and Albertus Denny Handoko *[c]

Close integration of metal nanoparticles (NPs) into a metal–organic framework (MOF) can be leveraged to achieve tailored functionality of the resulting composite structure. Here, we demonstrate a "ship-in-a-bottle" approach to produce ≈4.0 nm bismuth (Bi) NPs within a thiol-rich zirconium-based MOF of Zr-DMBD (DMBD = 2,5-dimercapto-1,4-benzenedicarboxylate). We found that the incorporation of Bi NPs into the Zr-DMBD framework relies on the free-standing thiol groups. These thiols have two roles – (i) aid in binding precursor Bi^{3+} preventing to form the insoluble bismuthyl unit (BiO^+) and (ii) controlling the growth of Bi NPs. The resulting composite, denoted as BiNP@Zr-DMBD-1, displayed enhanced catalytic activity due to strong interactions between Bi NPs and organic linkers mediated by sulfur, promoting charge transfer from the Bi NP to the MOF matrix. BiNP@Zr-DMBD-1 remained stable after CO_2 electroreduction to formate in a flow setting, with >88% faradaic efficiency at 25 mA cm^{-2} current density. Additionally, BiNP@Zr-DMBD-1 composite was shown to exhibit photoactivity beyond the typical near-UV absorption range of Bi NPs, where it completely degraded methylene blue dye within 1 h of blue LED irradiation. This work therefore underlines the potential of thiol-rich MOFs in developing new nanomaterials for diverse catalytic applications.

New concepts

Nanoparticles (NPs) of bismuth (Bi) are important for catalysis, magnetic, and biomedical application. However, ultrasmall Bi-NPs (∼10 nm or below) is very unstable due to tendency to oxidise and agglomerate. Metal–organic frameworks (MOFs) provide a platform for incorporating NPs within their structures. Surprisingly, examples of Bi-NPs MOFs are scarce. To address these issues, we introduce a "ship-in-a-bottle" strategy to synthesize ultrasmall Bi NPs within Zr-DMBD, a thiol-rich zirconium-based MOF. Unlike previous studies where Bi NPs were merely adsorbed onto MOF surfaces, our approach utilizes Hard–Soft Acid–Base (HSAB) concept to directly integrate Bi-NPs into the Zr-DMBD framework. The soft thiol groups bind to Bi^{3+} ions, preventing the formation of insoluble bismuthyl units (BiO^+) and controlling nanoparticle growth. The resulting BiNP@Zr-DMBD-1 shows strong chemical bonding between Bi NPs and the MOF, that also enhances charge transfer. As a result, our BiNP@Zr-DMBD-1 excels over common Bi and Bi-chalcogenides in both electrocatalysis, selectively reducing CO_2 to formate, and photocatalysis, with excellent visible light photoactivity. This work significantly advances MOF-based nanomaterials by demonstrating a method to achieve stable, chemically bonded NPs that can be extended to other soft metals within thiol-rich MOFs.

1. Introduction

The integration of metal nanoparticles (NPs) into metal–organic frameworks (MOFs) has yielded noteworthy breakthroughs in diverse applications such as catalysis, sensing, and energy storage.[1–5] There are two predominant methodologies to incorporate NPs into MOFs. The first is a 'ship-in-a-bottle' approach, where the MOF is impregnated with a metal salt solution followed by its treatment with reducing agents to reduce the metallic cations to the elemental state.[6–10] The second method is known as the 'bottle-around-the-ship' approach where the MOF is assembled around a pre-synthesized metal NP seed.[5,11–16] While both processes have their respective advantages, they face common challenges: including agglomeration of NPs, phase separation between NPs and MOFs, as well as degradation of the MOFs' crystallinity, surface areas, and porosity. Additionally, direct carbonization of a MOF under inert atmosphere is another bottom-up approach to obtain nanoparticles encapsulated in carbonized material where high-cost MOF acts as the precursor/template.[17] Arguably, keeping the NPs within the MOF channels is more favorable, as the unique

---

[a] *Institute of Materials Research and Engineering (IMRE), Agency for Science, Technology and Research (A*STAR), Singapore 138634, Republic of Singapore. E-mail: parijat_borah@imre.a-star.edu.sg, zhengtao@imre.a-star.edu.sg*

[b] *Department of Chemistry, University College London, 20 Gordon St., WC1H 0AJ, London, UK*

[c] *Institute of Sustainability for Chemicals, Energy and Environment (ISCE2), Agency for Science, Technology and Research (A*STAR), 1 Pesek Road, Jurong Island, Singapore 627833, Republic of Singapore. E-mail: handoko_albertus@isce2.a-star.edu.sg*

† Electronic supplementary information (ESI) available. See DOI: **https://doi.org/10.1039/d4mh01153h**

‡ These authors contributed equally to this work.

nano-reticular chemistry of the MOF as well as the NP–MOF interactions can be leveraged to enable precise control over the size, distribution and functionality of the embedded NPs.[1,3]

However, achieving both seamless NP–MOF integration and desirable composite properties is challenging. Thus, innovative strategies and a clearer understanding of the metal-MOF incorporation mechanisms are needed. Up to now, various mono- or bi-metallic nanoparticles, including Au, Pt, Pd, Co, Ni, *etc.* have been incorporated into various MOF matrices.[1,3,5] On the other hand, bismuth (Bi) has recently garnered attention in the electrochemical reduction of CO_2 (CO_2RR) to formate due to its high efficiency, low toxicity, abundance, stability, and cost-effectiveness.[18] To date, various Bi-based catalysts with diverse morphologies and compositions have been developed, including single atomic Bi,[19] Bi nanoparticles,[20–23] Bi nanobelts,[10] Bi nanowires,[24] Bi_2O_3 nanotubes,[25] and bismuthene.[26] However, these Bi electrocatalysts often require large overpotentials or exhibit low current densities, limiting their practical applications in CO_2RR. To tackle these challenges, several Bi-MOF-based electrocatalysts with designed Bi nanostructures featuring abundant corners and edges have been developed.[19,27–31] It's worth noting that these Bi-MOFs often need to be pyrolyzed to form BiNP/carbon composites, which destroys the precious organic building blocks, diminishes the crystallinity and total surface area/porosity, and leads to uncontrolled aggregation of BiNP, possibly also causing undesirable evaporation of Bi during the pyrolysis process.[19,30,31] Not surprisingly, examples of MOF-incarcerated Bi NPs are scarce due to inherent challenges such as high instability of Bi NPs, tendency for Bi NP agglomeration, and susceptibility of Bi to be oxidized to its ionic state. Furthermore, the ''ship-in-a-bottle'' method requires the host MOF must exhibit several essential properties: (i) the framework should provide sites that enable uniform uptake of metal ion precursors, (ii) it should permit precise control over nanoparticle formation, and (iii) it must maintain stability throughout post-synthetic processing. Recently, Wu *et al.* overcame these challenges by introducing Bi NPs into a zirconium-based porphyrin MOF, PCN-222, employing a 'ship-in-a-bottle' approach.[32] The resulting Bi-PCN-222 composite exhibited excellent self-bacteria-killing and wound-healing properties. Despite the strong interaction observed between the MOF and Bi NPs, there was no distinct chemical bonding between the organic linker and the Bi NPs. As a result, Bi NPs were absorbed on the surface of nanocubes of PCN-222. The establishment of strong interactions between the metal nanoparticles (NPs) and organic linkers is crucial not only to enhance electron transfer within the host network but also to stabilized metal NPs inside the MOF matrix. In this study, we present a 'ship-in-a-bottle' approach to incarcerate Bi NPs into Zr-DMBD (DMBD = 2,5-dimercapto-1,4-benzenedicarboxylate), a thiol(–SH)-rich Zr-based UiO-66 type MOF, with strong electronic interactions between NPs and MOF matrix primarily *via* metal–thiolate bonds (Fig. 1).[33] The linker molecule, H_2DMBD (2,5-dimercapto-benzenedicarboxylic acid), combines hard and soft properties based on the hard and soft acids and bases theory, with carboxyl groups (hard) and thiol groups (soft). The chemically hard Zr^{4+} ion preferentially binds with the 'hard' carboxyl groups, resulting in an open MOF (Zr-DMBD) with densely arranged free-standing –SH groups that offer unique advantages. For instance, thiols as strong soft donors readily take up various metal ions,[33–38] (*e.g.*, mimicking the iron–sulfur, copper–sulfur proteins) within the MOF matrices. Our strategy based on the strong affinity of soft thiol groups for Bi^{3+} ions, leading to homogeneously distributed Bi-thiolate units within the porous Zr-DMBD framework (Fig. 1). Furthermore, the Bi-thiol interaction is pivotal in controlling the growth of Bi NPs within the crystalline nanoporous MOF during subsequent reduction steps. Additionally, Zr-DMBD stands out for its exceptional stability in water and common organic solvents, even under acid/mild base conditions.[33,37,39,40] The unique synergy between hard-and-soft design and stability of Zr-DMBD was thus instrumental in enabling the encapsulation of these challenging Bi NPs within MOF particles through a straightforward ''ship-in-a-bottle'' approach. Recent evaluations of a Bi(III) ion-loaded Zr-DMBD for CO_2RR to formic acid (FA) revealed that metallic Bi generated *in situ* was the active catalyst.[41] Therefore, we envisaged the potential of our novel BiNP@Zr-DMBD as an efficient electrocatalyst for CO_2RR to FA. As anticipated, BiNP@Zr-DMBD demonstrated excellent electrocatalytic efficacy with high Faradic efficiency (FE) and high selectivity towards formate.

Just like noble metals, Bi nanoparticles have plasmonic properties that are highly influenced by their particle sizes and the dielectric environment.[42,43] For example, small Bi NPs (with diameters ≤20 nm) exhibit absorbance in the (near) UV region, especially around 400 nm.[44] Since only about 4% of sunlight consists of UV light, there has been ongoing research to create bismuth-based photocatalysts that can perform under visible light, which makes up 42% of the solar irradiance spectrum, such that solar energy can be effectively harnessed for photocatalytic applications. This research includes exploring

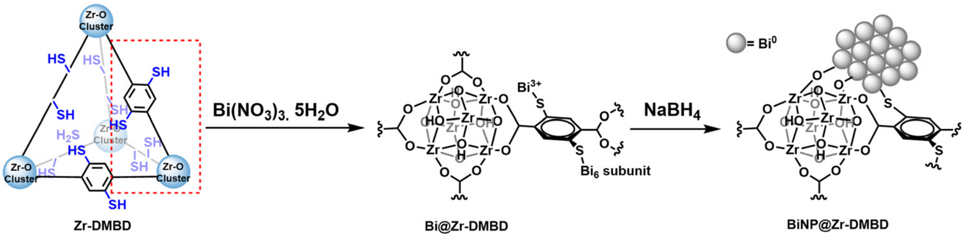

Fig. 1 Schematic presentation of chemical transformation of Zr-DMBD to BiNP@Zr-DMBD.

materials like bismuth tungstate,[45,46] bismuth oxyhalides,[47–50] bismuth ferrite,[51] and composites with graphene oxides,[52] among others. Many scientists have been interested in enhancing the performance of MOFs (*e.g.*, HKUST, UiO-66 *etc.*) by combining them with substances like Bi_2O_3 or $BiVO_4$, aiming to improve their ability to use visible light for photocatalysis.[53] In this context, we showcase the utilization of BiNP@Zr-DMBD as a photocatalyst and assess its effectiveness in the degradation of model organic compounds such as methylene blue under visible light.

2. Experimental section

2.1. Synthesis of Zr-DMBD

Typically, a 250-mL Schlenk tube loaded with 2,5-dimercapto-1,4-benzenedicarboxylic acid (H_2DMBD 198.6 mg, 0.87 mmol) was evacuated and refilled with N_2 for 3 times. The DMF (dimethylformamide, 32 mL) solution of $ZrCl_4$ (204.0 mg, 0.87 mmol) and acetic acid (7872.0 mg, 131.20 mmol) was bubbled with N_2 gas for 5 min and then transferred into the Schlenk tube under N_2 protection. The Schlenk tube was capped tightly and placed into a 120 °C oil-bath for 24 h. After the solution was cooled down slowly to room temperature, the resultant precipitate was collected by centrifugation, washed by DMF (15 mL, three times), DCM (dichloromethane, 15 mL, three times), and solvent exchange with acetone for one day. Finally, sample was dried under N_2 flow to obtain as-synthesized Zr-DMBD as a slightly yellow colored powder.

2.2. Synthesis of Bi@Zr-DMBD

In a typical synthesis, 10 mL of aqueous $Bi(NO_3)_3{\cdot}5H_2O$ was prepared at a concentration of 10 mM, and the solution was maintained at pH 2 using HNO_3. To this acidic solution, 100 mg of Zr-DMBD was added. The resultant mixture was stirred overnight at room temperature. Afterward, the solid was isolated by centrifugation, washed with H_2O (10 mL, pH 2, three times), then soaked in DI water for a day and centrifuged to replace the water three times. This solid sample was washed with ethanol (10 mL, three times) before immersing in acetone (replaced solvent three times in random intervals) for one day for solvent exchange. Finally, sample was dried under vacuum for 24 h to obtain as-synthesized Bi@Zr-DMBD as orange solid powder.

2.3. Synthesis of BiNP@Zr-DMBD

In a typical synthesis, 60 mg of Bi@Zr-DMBD was dispersed in 10 mL of ice-cold DI water and the mixture was stirred in an ice bath for 30 min. To this, 2 mL of ice-cold aqueous $NaBH_4$ (1 M) was added dropwise and the reaction mixture was stirred at room temperature for 15 min. Afterward, the solid was isolated by centrifugation, washed with H_2O (10 mL, three times), and then with ethanol (10 mL, three times). The sample was immersed in acetone (replaced solvent three times in random intervals) for one day for solvent exchange. Finally, the solids were dried under vacuum for 24 h at room temperature to obtain as-synthesized BiNP@Zr-DMBD-1 as dark green solid powder. Following the same protocol, black colored BiNP@Zr-DMBD-2 was synthesized using 4 ml of aqueous $NaBH_4$ (1 M).

3. Results and discussions

3.1. Metalation of Zr-DMBD: synthesis and characterization

To start with, a light yellow colored solid of Zr-DMBD was synthesized following the previously reported procedure.[37] The structure of as-synthesized Zr-DMBD was confirmed by comparing the powder X-ray diffraction (PXRD) pattern and Fourier-transform infrared spectroscopy (FT-IR) spectrum with previously reported results (pattern (i) in Fig. 2a, b and c).[33,37] The distinct PXRD peaks of Zr-DMBD revealed that it is isostructural with the reported UiO-66, which contains linear 1,4-benzenedicarboxylate struts and $Zr_6O_4(OH)_4$ clusters as 12-connected nodes.[54] Furthermore, quantitative refinements of the Zr-DMBD PXRD matches well with the closest Zr-DMBD structure based on UiO-66(SH)$_2$ (Fig. S2b, ESI†).[55] The solid Zr-DMBD sample was subjected to elemental and inductively coupled plasma (ICP) elemental analyses; leading to a composition of $Zr_6O_4(OH)_4{\cdot}(C_8H_2O_4S_2)_6{\cdot}(DMF){\cdot}(H_2O)_{14}$ (Table S1, ESI†). Based on this composition, the ligand accounts for 70% of the total weight, which is consistent with the TGA analysis (Fig. S11, ESI†). In aqueous environments, Bi^{3+} ions can rapidly transform into insoluble bismuth hydroxide or bismuth oxides

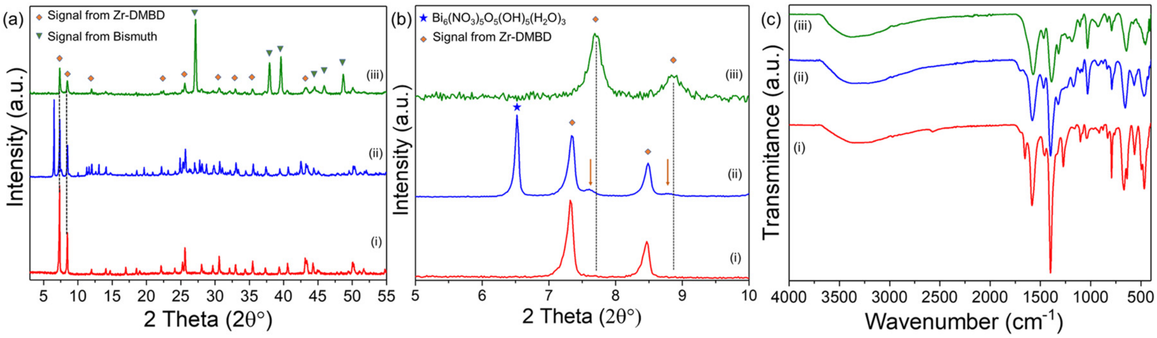

Fig. 2 (a) X-ray powder patterns of (i) Zr-DMBD, (ii) Bi@Zr-DMBD, and (iii) BiNP@Zr-DMBD-1; (b) enlarged version of PXRD of (i) Zr-DMBD, (ii) Bi@Zr-DMBD, and (iii) BiNP@Zr-DMBD-1; (c) FT-IR spectra of (i) Zr-DMBD, (ii) Bi@Zr-DMBD, and (iii) BiNP@Zr-DMBD-1.

at neutral or high pH levels.[56] To circumvent this intrinsic problem, the orange solids of Bi@Zr-DMBD was synthesized by treating Zr-DMBD with a 10 mM aqueous solution of $Bi(NO_3)_3 \cdot H_2O$ at pH 2 in an overnight reaction at room temperature (see Fig. 1).[57] The PXRD pattern of Bi@Zr-DMBD showed all the crystalline planes of Zr-DMBD along with several new planes attributed to thiolate-anchored crystalline Bi_6 subunits similar to $[Bi_6(NO_3)_5(OH)_3(O)_5] \cdot 3H_2O$ (PDF 04-012-8486) (Fig. S26 in the ESI†). On the other hand, the FT-IR spectrum of Bi@Zr-DMBD demonstrated that the distinct stretching vibration of S–H at 2573 cm^{-1} disappeared after metalation indicating the formation of S–Bi bond *via* S–H bond cleavage (Fig. 2c and Fig. S1a, ESI†).[37] The sulfur–bismuth bond exhibits high thermal and hydrolytic stability and can control high coordination capacity of the bismuth center.[56] Consequently, bismuth-thiolate interaction in Bi@Zr-DMBD prevented the intermolecular interactions and polymerization of Bi^{3+} to form the bismuthyl unit (BiO^+), which essentially precipitates quantitatively. The energy-dispersive X-ray spectroscopy (EDX) elemental mapping of Bi@Zr-DMBD revealed the homogeneous distribution of Bi in the crystals Zr-DMBD together with other key constituent elements such as of S, O, and Zr (Fig. S4, ESI†). We also employed XPS to confirm the compositions of MOF materials, showing the existence of C, O, S, Zr, and Bi elements in Bi@Zr-DMBD which is consistent with the EDX mapping (Fig. S25(ii), ESI†). Since these studies didn't provide the evidence of elemental N from nitrate, we believe that amount of Bi_6 subunit is significantly low and primarily presents inside the MOF matrix. Additionally, the PXRD pattern of Bi@Zr-DMBD showed appearance of small broad and right-shifted satellite peaks of (111) and (200) planes centered at $2\theta = 7.6°$ and 8.8° respectively attributed to cell contraction by partial structural change by the small quantity of thiol anchored crystalline Bi_6 subunits inside the porous MOF matrix (Fig. 2b). The ICP analysis showed a Zr/Bi ratio of 6.0 : 4.1. The N_2 adsorption isotherm of Bi@Zr-DMBD at 77 K exhibited a typical type-I isotherm with a Brunauer–Emmett–Teller (BET) surface area of 263 $m^2\ g^{-1}$, which is smaller than the that of Zr-DMBD (413 $m^2\ g^{-1}$). The BJH desorption pore size distribution indicated that the pore size of Zr-DMBD was distributed at around 1.3, and 2.5 nm, especially predominately distributed around 1.3 nm, which was reduced drastically in Bi@Zr-DMBD indicating the occupancy of Bi inside the pores of MOF matrix (Fig. S7, ESI†). However, the scanning electron microscopy (SEM) images showed that the morphology of Zr-DMBD retained in Bi@Zr-DMBD after metalation, although the average size of the particles was reduced slightly (Fig. S9, ESI†). The FT-IR spectra of Bi@Zr-DMBD showed the presence of two strong signals at 1580 and 1399 cm^{-1} due to the asymmetric and symmetric stretching of carboxylic (O–C=O) group respectively and three characteristic bands at 565 cm^{-1}, 470 cm^{-1}, and 667 cm^{-1} attributed to the Zr–O(C) and Zr–O stretching frequencies respectively (Fig. 2c and Fig. S1b, ESI†).[58,59] These results thus corroborate that the connection between organic linker and Zr–O cluster remained intact after metalation by Bi in Bi@Zr-DMBD.

3.2. MOF-incarcerated Bi NPs: synthesis and characterization

Bi NPs inside the MOF matrix was synthesized by reducing orange colored Bi@Zr-DMBD using two different amounts of aqueous solution of $NaBH_4$ as described in the experimental section to obtain BiNP@Zr-DMBD-1, and BiNP@Zr-DMBD-2 as dark green and black colored solids respectively. The PXRD patterns of both samples showed characteristic diffraction peaks of metallic Bi indicating effective reduction of Bi^{3+} to Bi^0 (Fig. S10, ESI†). Dark green BiNP@Zr-DMBD-1 also exhibited two characteristic signals originating from Zr-DMBD (111) and (200) planes, indicating that the crystalline order of the cubic net was maintained (Fig. 2a and Fig. S10, ESI†).[33] On the other hand, the crystallinity of the MOF completely vanished in the black solids of BiNP@Zr-DMBD-2 (Fig. S10, ESI†). Transmission electron microscope (TEM) micrographs of BiNP@Zr-DMBD-1 showed that Bi NPs with average size of ≈ 4 nm was successfully formed *inside* the MOF crystals (Fig. 3). These Bi NPs had a lattice spacing of about 0.33 nm that corresponded to the (012) plane of the Bi NPs (Fig. 3c).[32] Furthermore, no Bi NPs were detected outside of the MOF crystals, indicating that all Bi NPs had been incarcerated into the Zr-DMBD framework. EDS element mapping showed that the Bi NPs obtained by reduction were evenly distributed within the MOF (Fig. S5, ESI†). It is important to mention that the PXRD pattern of BiNP@Zr-DMBD-1 showed peak broadening and shifting towards higher 2θ that could have arisen from a partial change of the structure and cell contraction, respectively, due to the confinement of Bi NPs inside the porous MOF matrix (Fig. 2).

BiNP@Zr-DMBD-1 was subjected to further CHNS, ICP, and gas absorption analyses to probe the formation and

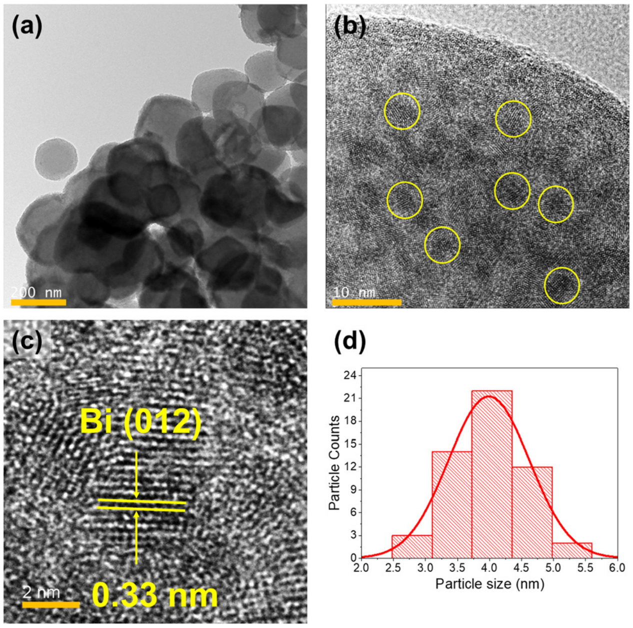

Fig. 3 (a)–(c) Transmission electron micrographs of BiNP@Zr-DMBD-1 at different scales and (d) the respective particle size histogram of 60 particles.

incarceration of BiNP. ICP determined the bulk Zr/Bi ratio to be 6.0 : 4.4 (Table S1, ESI†), coupled with CHNS results, an empirical composition of $Zr_6O_4(OH)_4\cdot(C_8H_2O_4S_2)_{4.5}\cdot(DMF)_{0.03}\cdot(H_2O)_{16}\cdot Bi_{4.4}$ is proposed. Based on this composition, the ligand constitutes 35% of the total weight that shows an approximate 25% loss of linker molecules from the original Zr-DMBD aligning with TGA analysis (Fig. S11, ESI†). A decrease in BET surface area to 199 $m^2\ g^{-1}$ (Fig. S6, ESI†) was also observed compared to pristine Zr-DMBD, alongside a notable reduction in micropores and the appearance of a broad distribution of mesopores (>4 nm) in the BJH pore size distribution profile of BiNP@Zr-DMBD-1 (Fig. S7, ESI†). Taken together these data, our findings suggest that nucleus of Bi NPs initially formed within the micropores of Zr-DMBD. As the Bi NPs grew, we posit that partial framework collapse may occur, creating larger voids (mesopores) within the MOF matrix to accommodate the NPs causing significant pore blockages that is also manifested in the low-pressure hysteresis in the N_2 desorption isotherm of BiNP@Zr-DMBD-1 (Fig. S6, ESI†). Such partial framework collapse has been demonstrated previously on AuNPs/MIL-101 *via* controlled thermal treatment.[60] There, the authors detected partial de-ligandation that afforded stronger interaction between the metal NPs to the inorganic nodes, while retaining some framework structure of the original MIL-101. On the other hand, when the amount of reducing agent used was too much, such as in the case for BiNP@Zr-DMBD-2, further separation of metallic Bi from the porous network of Zr-DMBD occurred, leading to a bulk formation of metallic Bi structure. This process led to significant structural collapse of the Zr-DMBD framework, leaving behind a hollow MOF residue and a high degree of phase separation between the metallic Bi and the MOF, as observed in the TEM images (Fig. S12, ESI†).

The FT-IR spectrum of BiNP@Zr-DMBD-1 demonstrated distinct bands in the wavenumber range of 1600 cm^{-1} to 1300 cm^{-1} corresponding to carboxylate vibration, signifying the presence of the DMBD linker (Fig. 2 and Fig. S1, ESI†). Although EDX element mapping revealed sulfur as one of the key constituents of BiNP@Zr-DMBD-1 (Fig. S5, ESI†), the stretching vibration of S–H remained absent (Fig. S1, ESI†), suggesting that the sulfur was likely coordinated with Bi.

Concurrently, we synthesized BiNP@UiO-66, aiming to integrate Bi NPs within the sulfur-free UiO-66 framework using a similar approach employed for BiNP@Zr-DMBD-1. XRD analysis revealed the presence of metallic Bi(0) phase alongside the crystalline cubic network of UiO-66 (Fig. S10, ESI†). However, TEM analysis indicated the formation of Bi NPs with an average diameter exceeding 100 nm on the surface of UiO-66 (Fig. S13, ESI†). This phase segregation can be attributed to the lack of free thiols within UiO-66 to serve as anchors and to regulate the controlled growth of ultra-small Bi NPs, as observed in the case of BiNP@Zr-DMBD-1. Furthermore, in the case of UiO-66, Bi^{3+} precursors that are physically absorbed can readily migrate and aggregate into larger Bi nanoparticles on the surface following $NaBH_4$ reduction.

X-ray photoelectron spectroscopy (XPS) was employed to examine the oxidation states of Bi in both Bi@Zr-DMBD and BiNP@Zr-DMBD-1 (Fig. 4). In the Bi@Zr-DMBD sample, the Bi 4f spectrum revealed two distinct peaks at 164.8 and 159.5 eV, which correspond to Bi^{3+} $4f_{5/2}$ and Bi^{3+} $4f_{7/2}$, respectively (Fig. 4a).[61] In the case of BiNP@Zr-DMBD-1, the binding energies of the constituent peaks of Bi 4f were found to be slightly lower at 163.1 and 157.7 eV, which are closer to the binding energies of the Bi^0 $4f_{5/2}$ and Bi^0 $4f_{7/2}$ states, respectively, which suggests the presence of metallic Bi (Bi^0) in BiNP@Zr-DMBD-1 (pattern (iii) in Fig. 4a).[61,62]

It is worth noting that the S 2p signal was obscured by the Bi 4f spectrum in both Bi@Zr-DMBD and BiNP@Zr-DMBD-1, despite being distinctly present at a binding energy of 163 eV in Zr-DMBD (pattern (i) in Fig. 4a). These results revealed a reduction of the Zr 3d binding energy upon the addition of Bi (Fig. 4b). This observation suggests that the inclusion of Bi NPs into Zr-DMBD enhances the electron density of Zr clusters, thus initiating a charge transfer from Bi NPs to the MOF. Consequently, the binding energy of Bi 4f in BiNP@Zr-DMBD-1 appeared higher than that of typical metallic Bi^0.[63] Moreover, the FTIR analysis of BiNP@Zr-DMBD-1 displayed broadened Zr–O(C) and Zr–O bands, along with a decrease in these stretching frequencies, indicating that the coordination environment of the Zr-oxo clusters had been altered (Fig. S1b, ESI†). Additionally, the

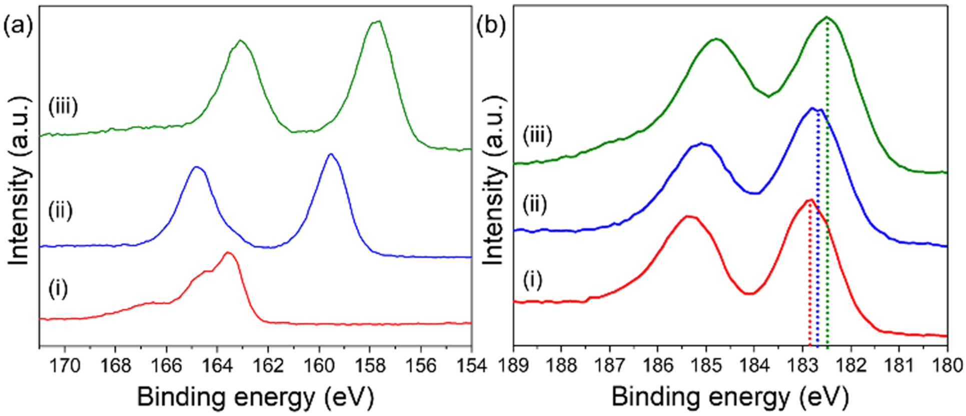

Fig. 4 (a) High-resolution XPS spectra in the region of Bi 4f for (i) Zr-DMBD, (ii) Bi@Zr-DMBD, and (iii) BiNP@Zr-DMBD-1. (b) High-resolution XPS spectra in the region of Zr 3d for (i) Zr-DMBD, (ii) Bi@Zr-DMBD, and (iii) BiNP@Zr-DMBD-1.

O 1s spectrum of BiNP@Zr-DMBD-1 displayed constituent peaks related to O–C═O, C–O–Zr, and Zr–O–Zr bonding, but with lower binding energies compared to Zr-DMBD (Fig. S14, ESI†), likely due to enhanced electron transfer between Bi and Zr. This could have resulted from the strong interactions between the Bi NPs and the Zr–O clusters of the MOF, where the O atoms play the role of facilitating the electron transfer between Bi and Zr. Data from repeated synthesis and characterization consistently demonstrated comparable atomic compositions and structural properties, further confirming the reproducibility of BiNP@Zr-DMBD-1. References from the literature also support the feasibility of achieving stable and reproducible outcomes in similar systems, addressing concerns about practical applications.[64,65]

3.3. Electrochemical CO_2 reduction

The CO_2RR performances of BiNP@Zr-DMBD-1 and BiNP@Zr-DMBD-2 were first examined using conventional H-Cell with static electrolyte and flowing CO_2 gas. Cathodic voltage was varied from −0.8 V to −1.4 V (*vs.* RHE), and the gas and liquid products were quantified. Both BiNP@Zr-DMBD-1 (Fig. 5a) and BiNP@Zr-DMBD-2 (Fig. 5b) demonstrate the expected affinity towards formate CO_2RR product, with H_2 being the main side product alongside small amounts of CO, methane, ethylene, and ethane. BiNP@Zr-DMBD-1 displayed superior formate selectivity and turnover at more cathodic potential. Specifically, at −1.4 V, the faradaic efficiency of formate ($FE_{Formate}$) and $j_{Formate}$ were steady above 60% and -2.2 mA cm^{-2} respectively. In comparison, the $FE_{Formate}$ at −1.4 V for BiNP@Zr-DMBD-2 dropped below 48%, with a concurrent elevation in H_2 production to around 20%. Electrochemically active surface area (ECSA) measurements revealed a slightly larger double layer capacitance on BiNP-Zr-DMBD-1 (2.3×10^{-5} mF cm^{-2}) compared to BiNP-Zr-DMBD-2 (1.9×10^{-5} mF cm^{-2}, Fig. S16b, ESI†), which could not account for the activity differences. We posit that the superior CO_2RR to formate in BiNP@Zr-DMBD-1 is linked to the smaller and more evenly distributed Bi NPs within the Zr-DMBD framework (Fig. 3) in contrast to BiNP@Zr-DMBD-2 where large Bi agglomerates were formed outside the MOF (Fig. S12, ESI†). As further comparison, CO_2RR were also performed using Bi@Zr-DMBD (unreduced Bi^{3+} state) and BiNP@UiO-66 (BiNP was on the surface of a sulfur free MOF). Both of these additional samples were inferior to BiNP@Zr-DMBD-1, in particular at more cathodic potential of −1.4 V due sudden increase in H_2 and CO evolution (Fig. S29, ESI†). These results indicated that the presence of ultra small BiNP stabilized by thiol groups is important to achieve high $FE_{Formate}$ and to suppress HER.

The better performing catalyst BiNP@Zr-DMBD-1 was then applied to flow cell configuration to demonstrate its applicability to larger scale CO_2RR. At −25 mA cm^{-2} applied current, BiNP@Zr-DMBD-1 produces formate with over 88.1% selectivity (Fig. 5c), equivalent to >22 mA cm^{-2} $j_{Formate}$ turnover. The higher FE can be attributed to the higher availability of CO_2 near the catalyst and a more stable bulk pH in the cathode compartment due to the larger electrolyte reservoir volume.

Further investigation using electrochemical impedance spectroscopy (EIS) at varying DC bias from 0 V to −1.6 V were then performed to probe the charge transfer kinetics at CO_2RR relevant potentials (Fig. S17, ESI†). Closer inspection of individual Nyquist plots reveals three time-constant components. The component at higher frequency (100 kHz to 1 kHz) is attributed to external parasitic effect as it does not change with external DC bias (Fig. S17b, ESI†). Fitting of the EIS data was then done using modified Armstrong equivalent circuit for multi-step reaction of one adsorbed intermediate,[66,67] with an additional R/C pair to represent external parasitic component at high frequency (Fig. S17c, ESI†). The fitting revealed consistently smaller charge transfer resistances (R_p and R_4, Fig. 6a and b) and higher admittance (Y_{05} and Y_{07}, Fig. 6c and d) for BiNP@Zr-DMBD-1 compared to BiNP@Zr-DMBD-2 at CO_2RR relevant cathodic potentials in both low and high frequency ranges. It should be noted that R values in general reflect the electrode kinetics, while Y is correlated with charges around the electrode.[66] The higher frequency R_p and Y_{05} components are commonly attributed to the double layer while the lower frequency R_4 and Y_{07} (<1 Hz) to surface adsorption/reaction.[67] The fact that BiNP@Zr-DMBD-1 shows lower R and higher Y at

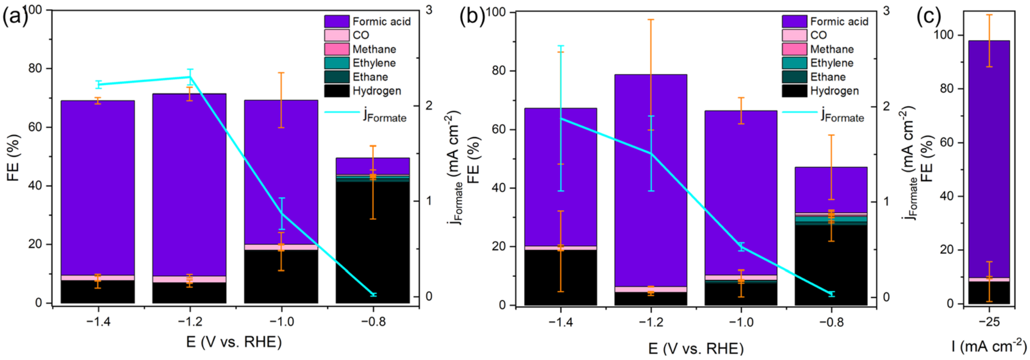

Fig. 5 Faradaic efficiencies (FE) of CO_2RR products along with formate partial current density (cyan lines) for (a) BiNP@Zr-DMBD-1 and (b) BiNP@Zr-DMBD-2 electrocatalyst in static H-cell configuration at fixed applied voltage as marked. (c) FE of CO_2RR products of BiNP@Zr-DMBD-1 in flow cell configuration at fixed −25 mA cm^{-2} input current. Vertical orange and cyan bars represent standard deviations of FE and partial current density respectively from 3 independent measurements.

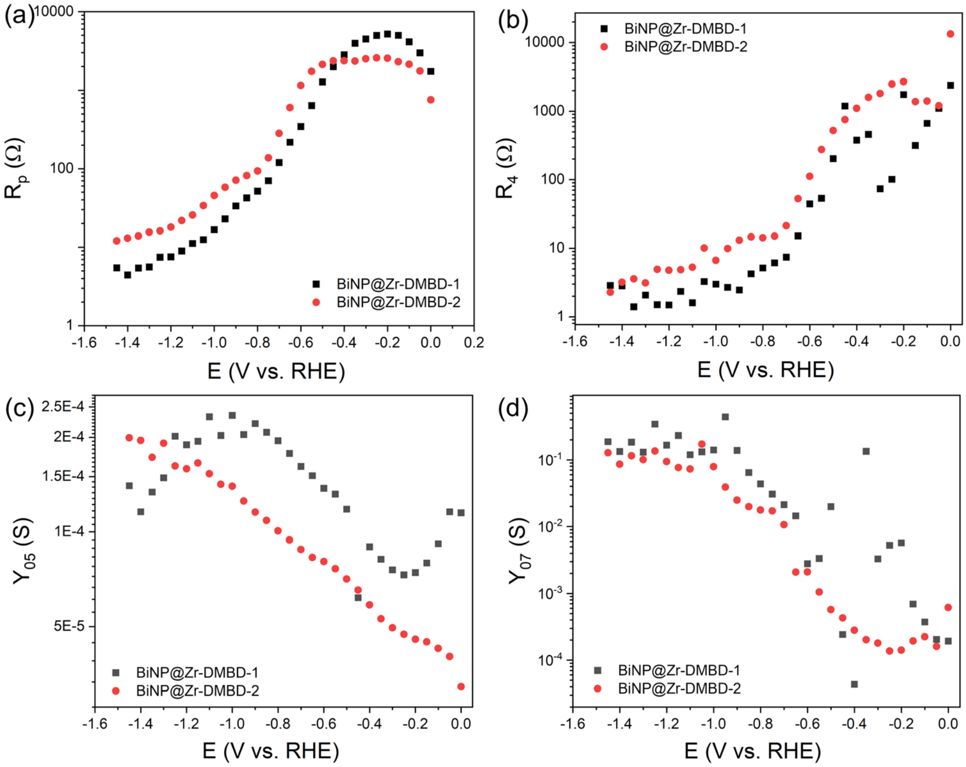

Fig. 6 Charge transfer resistance comparison between BiNP-Zr-DMBD-1 and BiNP-Zr-DMBD-2 at (a) intermediate frequency of 10 Hz to 1 kHz (R_p) and (b) low frequency of <1 Hz (R_4). Admittance comparison of the representative pseudocapacitance element at (c) intermediate frequency of 10 Hz to 1 kHz (Y_{05}) and (d) low frequency of <1 Hz (Y_{07}). EIS fitting was done using modified Armstrong equivalent circuit for multi-step reaction of one adsorbed intermediate. More details are available in ESI.†

both frequencies indicate that the superior CO_2RR activity is not only caused by higher availability of active surface area, but also more facile intermediate adsorption over BiNP@Zr-DMBD-2. At frequency similar to catalysis turnover (<1 Hz), R_4 and Y_{07} are relevant metrics to reflect the intrinsic adsorption behavior and electrocatalytic activity.[68] However, precise measurements of these metrics at catalytically relevant potentials are challenging due to the vigorous product evolution leading to turbulent EIS data and higher numerical fitting uncertainty (Fig. S17e, ESI†).

3.4. Post-catalysis characterization

The short-range crystalline environments of the MOFs pre- and post-electrochemical reduction were assessed using Raman spectroscopy to determine any *in situ* transformations of the crystalline bismuth phase. As-prepared BiNP@Zr-DMBD-1 shows the expected Raman bands around 67.5 and 93.7 cm^{-1} belonging to the A_g and E_{1g} modes of Bi^0 (Fig. 7a). Post CO_2RR characterization shows the similar bands of Bi^0 alongside two small peaks at 124 cm^{-1} and 310.5 cm^{-1}, which are attributed

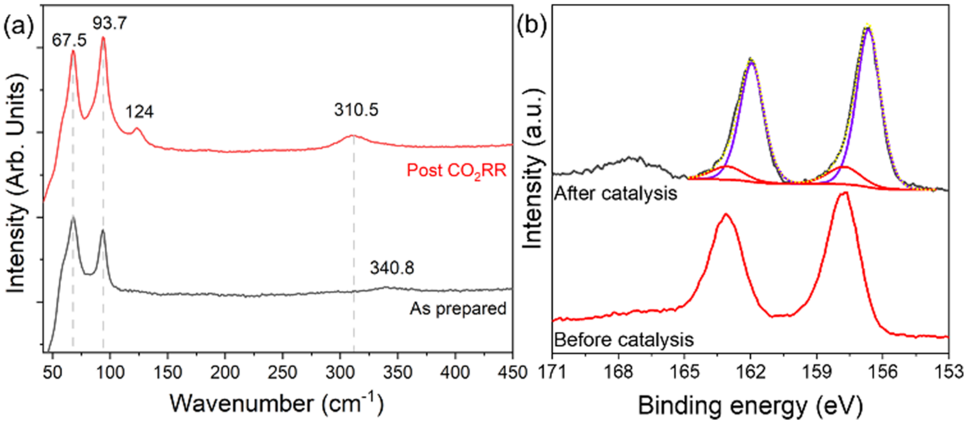

Fig. 7 Comparison of as-prepared and post CO_2RR characterization of BiNP-Zr-DMBD-1 (a) Raman spectra and (b) high resolution Bi 4f XPS. Broad peak around 168 eV on Post CO_2RR XPS spectra (black line) can be attributed to S 2s originating from the Nafion binder.

to a β-Bi_2O_3 phase that could have formed due to surface oxidation. The surface oxidation effect was much more pronounced in BiNP@Zr-DMBD-2, as seen from the more intense β-Bi_2O_3 peaks (Fig. S18, ESI†). XPS analysis performed on BiNP@Zr-DMBD-1 post-CO_2RR also revealed a 1.2 eV reduction in the BE of Bi^0 as shown in the Bi 4f spectra of BiNP@Zr-DMBD-1 before and after CO_2RR (Fig. 7b), indicating a reduction in the charge transfer from the Bi NPs to the MOF (Fig. 4a) after catalysis. This could likely be due to partial decomposition of the MOF matrix.

To further probe this observation, we conducted additional XPS elemental analysis of BiNP@Zr-DMBD-1 after a simulated CO_2RR process but without any interfering ionomer (Nafion). We found that while surface Bi to Zr ratio remained consistent post-CO_2RR condition (Table S2, ESI†), surface sulfur content in BiNP@Zr-DMBD-1 was significantly reduced following CO_2RR (Fig. S20, ESI†). While XPS finding suggests partial decomposition of the organic linkers from the MOF, we posit that the decomposition may be limited to the surface, as the sampling depth of XPS is very shallow and no notable morphological degradation was observed in recovered catalysts TEM post CO_2RR (Fig. S19, ESI†). This implies that the Bi nanoparticles can still be protected within the MOF structure, making the composite a more suitable catalyst for CO_2RR to formate compared to plain transition metal chalcogenides-based catalysts.[69,70] Our position is supported by the ICP result of post-CO_2RR bulk BiNP@Zr-DMBD-1, showing that the bulk Zr/Bi ratio was found to be practically the same at 1.4, indicating that Bi NPs can still be stabilized in the bulk (Table S2, ESI†).

3.5. Photocatalytic degradation of methylene blue

UV-visible diffuse reflectance spectroscopy (DRS) was employed to analyze the photo-absorption of the samples under investigation. In the UV/Vis DRS of Zr-DMBD (spectrum in red, Fig. 8a), absorption was observed within the range of 250 to 400 nm, with an absorption edge extending to 500 nm. Contrary to the typical behavior of Bi nanoparticles (NPs) with small diameters ($\leq$20 nm), which often exhibit absorption in the near-UV region,[44] the UV/Vis DRS of BiNP@Zr-DMBD-1 demonstrated a broad photo-absorption extending well into the visible light region (spectrum in blue, Fig. 8a) indicating improved efficiency in harnessing visible light. The presence of surface plasmonic resonance (SPR) attributed to the Bi NPs likely facilitated enhanced photo-absorption and energy transfer in the BiNP@Zr-DMBD-1 system, thereby benefiting the photocatalytic process.[50] The bandgap energy (E_g) value of BiNP@Zr-DMBD-1 was determined from the DRS data using the Kubelka–Munk function $F(R_\infty)$,[71] as represented by the following equation:

$$(F(R_\infty)\cdot h\nu)^{1/n} = A(h\nu - E_g) \tag{1}$$

where R_∞ is the reflectance of an infinitely thick specimen, $h\nu$ is discrete photon energy, and A is the proportionality constant. The factor n depends on the nature of the electron transition and is equal to 1/2 or 2 for direct and indirect transition band gaps, respectively. Our analysis revealed that Zr-DMBD has an indirect optical band gap energy of 2.8 eV which decreased to 2.5 eV following the incorporation of Bi NPs in BiNP@Zr-DMBD-1 (Fig. 8b). The lowering of the band gap energy thus suggests the potential for enhanced photocatalytic activity.

We then examined the photocatalytic efficacy of BiNP@Zr-DMBD-1 in the degradation of methylene blue (MB) dye when exposed to visible light (specifically, blue light). In the experimental setup, 5 mg of BiNP@Zr-DMBD-1 was dispersed in a 10 ml aqueous solution containing 25 ppm of MB dye, and the mixture was continuously stirred while being subjected to blue LED light exposure over a time interval of up to 60 min. Subsequently, the photodegraded samples were centrifuged to separate the supernatant for UV-vis absorption analysis. The UV-vis spectra (Fig. 9a) show a gradual reduction in MB concentration over a span of 60 min under these conditions, whereas negligible degradation of MB occurred without light exposure (Fig. S21, ESI†).

Next, the Langmuir–Hinshelwood (L–H) kinetic model (eqn (2)) was employed to study the pseudo first-order photocatalysis kinetics of the photocatalytic degradation of MB using BiNP@Zr-DMBD-1 as photocatalyst.

$$\ln(C_0/C) = kt \tag{2}$$

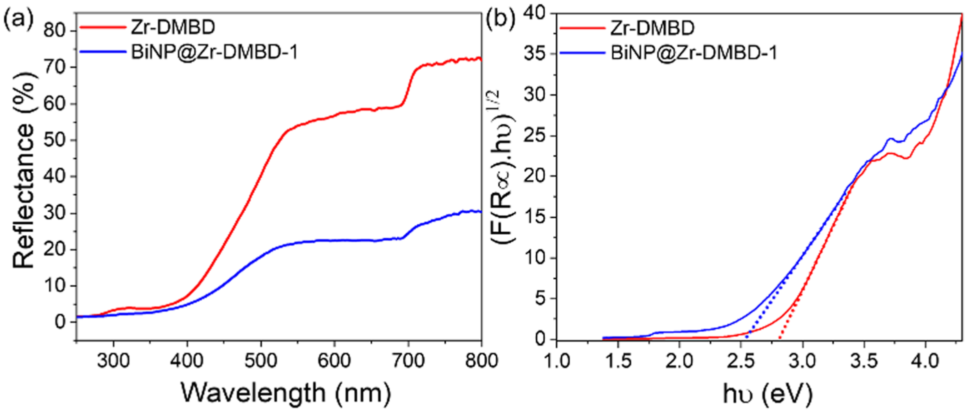

Fig. 8 (a) UV-Vis DRS of Zr-DMBD (red line) and BiNP@Zr-DMBD-1 (blue line). (b) Tauc plot of Kubelka–Munk function for bandgap determination of Zr-DMBD (red line) and BiNP@Zr-DMBD-1 (blue line).

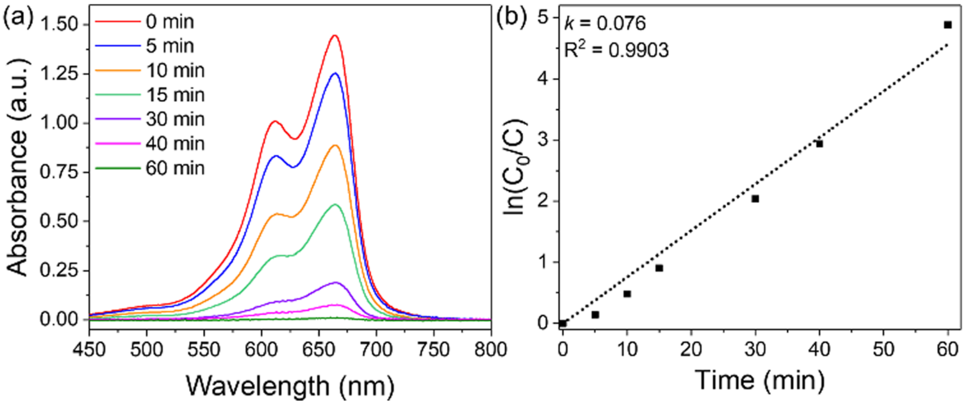

Fig. 9 Photodegradation of methylene blue using BiNP@Zr-DMBD-1 under visible light irradiation. (a) Raw UV-Vis adsorption analysis spectra and (b) the corresponding pseudo first-order rate constants according to the Langmuir–Hinshelwood kinetic model.

where C_0 and C are the initial concentration and concentration after time t respectively, and k is the rate constant of MB decomposition. The concentration of MB varies proportionally with the absorption value of its characteristic absorption peak at $\lambda_{\max}$ = 661 nm. Thus, in this study, the absorption value of 661 nm of the solution was used for the calculation of C_0/C. By plotting $\ln(C_0/C)$ *versus* t, we found the k of MB decomposition to be 7.6×10^{-2} min^{-1} for BiNP@Zr-DMBD-1 (Fig. 9b). This rate is 8.4 times faster than that of Zr-DMBD alone (Fig. S22, ESI†). This result indicates that Bi NPs significantly enhance the photocatalytic efficiency of BiNP@Zr-DMBD-1 under visible light. Furthermore, Fig. S23 (ESI†) illustrates the recovery and reusability of BiNP@Zr-DMDB-1 for up to three cycles, with no discernible decline in its photodegradation efficacy. The structural integrity of the recovered catalyst after three catalytic cycles were confirmed by powder XRD and BET surface area analyses (Fig. S27 and S28, ESI†). Radical trapping experiments were carried out to investigate the radical species involved in the photocatalytic degradation of MB. In these trials, isopropyl alcohol (IPA) was utilized as a scavenger for hydroxyl radicals ($^{\bullet}$OH), while benzoquinone (BQ) and formic acid (FA) were employed as scavengers for superoxide radicals ($^{\bullet}O_2^-$) and holes (h^+), respectively.[72] Results from these trials showed a significant contrast in the photocatalytic efficacy of BiNP@Zr-DMBD-1 in the presence and absence of various scavengers (Fig. S24, ESI†). The addition of FA had negligible impact on the photocatalytic decomposition of MB, suggesting that h^+ played a minor role in the oxidation process. Conversely, the presence of BQ significantly hindered the photocatalytic activity, indicating the involvement of $^{\bullet}O_2^-$ in MB degradation. Moreover, the introduction of IPA slightly impeded dye degradation due to the generation of a small quantity of $^{\bullet}$OH through the reaction of $^{\bullet}O_2^-$ with proton. Hence, this study demonstrated that near UV light-absorbing BiNP can be useful for various photocatalytic applications, such as water treatment under visible light, by incorporating them inside Zr-DMBD.

4. Conclusion

In summary, we present a "ship-in-a-bottle" strategy for embedding highly unstable ultrasmall bismuth nanoparticles (Bi NPs) within the network of Zr-DMBD, a thiol-rich MOF. The incorporation process crucially relies on the presence of free-standing sulfur, which plays a pivotal role in facilitating the binding of Bi(III) precursor and to regulate the growth of Bi NPs inside MOF particles. The strong interactions between the Bi NPs and organic linkers mediated by sulfur, promote electron transfer within the MOF matrix, enhancing the catalytic activity of resultant composite. BiNP@Zr-DMBD-1 exhibits excellent performance in CO_2 electroreduction to formate with over 88% FE at 25 mA cm^{-2} current density in a flow setting. Additionally, BiNP@Zr-DMBD-1 showcases efficient photocatalytic activity under visible light, extending the utility of Bi NPs beyond their typical near-UV absorption range. Notably, the composite maintains stability even after complete degradation of methylene blue dye under blue LED irradiation within 1 hour. This work opens new avenues for developing functional thiol-rich MOFs into new nanomaterials with diverse catalytic and photocatalytic applications.

Author contributions

Parijat Borah: conceptualization, data curation, formal analysis, funding acquisition, investigation, methodology, project administration, resources, supervision, validation visualization, writing – original draft. Natalie McLeod, Nipun Kumar Gupta, Reuben J. Yeo, Tanmay Ghosh, Lidao Li, Prajna Bhatt, Yuhan Liu and Robert Palgrave: data curation, formal analysis, investigation, validation, and writing – review & editing. Zainul Aabdin and Yee-Fun Lim: methodology, project administration, resources, software, supervision, validation, writing – review & editing, Zhengtao Xu and Albertus Denny Handoko: conceptualization, formal analysis, funding acquisition, project administration, resources, software, supervision, validation, visualization, and writing – original draft.

Data availability

The data supporting this article have been included as part of the ESI.†

Conflicts of interest

The authors declare that they have no known competing financial interests or personal relationships that could have appeared to influence the work reported in this paper.

Acknowledgements

This Research is supported by the RIE2020/RIE2025 Pitchfest, a career development fund SC25/23-830824, administered by A*STAR and ASEAN-India Collaborative R&D (AICRD) grant (CRD/2022/000533). A. D. H. acknowledges funding from A*STAR Horizontal Technology Coordinating Office (C231218004). Z. X. acknowledges a startup fund from A*STAR (SC25/22-119116). N. M. acknowledges support from A*STAR Research Attachment Programme (ARAP). XPS was carried out at HarwellXPS, the UK National XPS Facility (EP/Y023587/1).

References

1 J. Yu, C. Mu, B. Yan, X. Qin, C. Shen, H. Xue and H. Pang, Nanoparticle/MOF composites: preparations and applications, *Mater. Horiz.*, 2017, **4**, 557–569, DOI: 10.1039/C6MH00586A.

2 N. Wang, Q. Sun and J. Yu, Ultrasmall Metal Nanoparticles Confined within Crystalline Nanoporous Materials: A Fascinating Class of Nanocatalysts, *Adv. Mater.*, 2019, **31**, 1803966, DOI: 10.1002/adma.201803966.

3 Q. Wang and D. Astruc, State of the Art and Prospects in Metal–Organic Framework (MOF)-Based and MOF-Derived Nanocatalysis, *Chem. Rev.*, 2020, **120**, 1438–1511, DOI: 10.1021/acs.chemrev.9b00223.

4 L. Liu and A. Corma, Confining isolated atoms and clusters in crystalline porous materials for catalysis, *Nat. Rev. Mater.*, 2021, **6**, 244–263, DOI: 10.1038/s41578-020-00250-3.

5 J. Liu, T. A. Goetjen, Q. Wang, J. G. Knapp, M. C. Wasson, Y. Yang, Z. H. Syed, M. Delferro, J. M. Notestein, O. K. Farha and J. T. Hupp, MOF-enabled confinement and related effects for chemical catalyst presentation and utilization, *Chem. Soc. Rev.*, 2022, **51**, 1045–1097, DOI: 10.1039/D1CS00968K.

6 Q.-L. Zhu, J. Li and Q. Xu, Immobilizing Metal Nanoparticles to Metal–Organic Frameworks with Size and Location Control for Optimizing Catalytic Performance, *J. Am. Chem. Soc.*, 2013, **135**, 10210–10213, DOI: 10.1021/ja403330m.

7 X. Gu, Z.-H. Lu, H.-L. Jiang, T. Akita and Q. Xu, Synergistic Catalysis of Metal–Organic Framework-Immobilized Au–Pd Nanoparticles in Dehydrogenation of Formic Acid for Chemical Hydrogen Storage, *J. Am. Chem. Soc.*, 2011, **133**, 11822–11825, DOI: 10.1021/ja200122f.

8 N. Cao, L. Yang, H. Dai, T. Liu, J. Su, X. Wu, W. Luo and G. Cheng, Immobilization of Ultrafine Bimetallic Ni–Pt Nanoparticles Inside the Pores of Metal–Organic Frameworks as Efficient Catalysts for Dehydrogenation of Alkaline Solution of Hydrazine, *Inorg. Chem.*, 2014, **53**, 10122–10128, DOI: 10.1021/ic5010352.

9 B. Xia, N. Cao, H. Dai, J. Su, X. Wu, W. Luo and G. Cheng, Bimetallic Nickel–Rhodium Nanoparticles Supported on ZIF-8 as Highly Efficient Catalysts for Hydrogen Generation from Hydrazine in Alkaline Solution, *ChemCatChem*, 2014, **6**, 2549–2552, DOI: 10.1002/cctc.201402353.

10 H. Dai, B. Xia, L. Wen, C. Du, J. Su, W. Luo and G. Cheng, Synergistic catalysis of AgPd@ZIF-8 on dehydrogenation of formic acid, *Appl. Catal., B*, 2015, **165**, 57–62, DOI: 10.1016/j.apcatb.2014.09.065.

11 D.-W. Lim, J. W. Yoon, K. Y. Ryu and M. P. Suh, Magnesium Nanocrystals Embedded in a Metal–Organic Framework: Hybrid Hydrogen Storage with Synergistic Effect on Physi- and Chemisorption, *Angew. Chem., Int. Ed.*, 2012, **51**, 9814–9817, DOI: 10.1002/anie.201206055.

12 G. Lu, S. Li, Z. Guo, O. K. Farha, B. G. Hauser, X. Qi, Y. Wang, X. Wang, S. Han, X. Liu, J. S. DuChene, H. Zhang, Q. Zhang, X. Chen, J. Ma, S. C. J. Loo, W. D. Wei, Y. Yang, J. T. Hupp and F. Huo, Imparting functionality to a metal–organic framework material by controlled nanoparticle encapsulation, *Nat. Chem.*, 2012, **4**, 310–316, DOI: 10.1038/nchem.1272.

13 C. Rösler, D. Esken, C. Wiktor, H. Kobayashi, T. Yamamoto, S. Matsumura, H. Kitagawa and R. A. Fischer, Encapsulation of Bimetallic Nanoparticles into a Metal–Organic Framework: Preparation and Microstructure Characterization of Pd/Au@ZIF-8, *Eur. J. Inorg. Chem.*, 2014, 5514–5521, DOI: 10.1002/ejic.201402409.

14 Y. Huang, Y. Zhang, X. Chen, D. Wu, Z. Yi and R. Cao, Bimetallic alloy nanocrystals encapsulated in ZIF-8 for synergistic catalysis of ethylene oxidative degradation, *Chem. Commun.*, 2014, **50**, 10115–10117, DOI: 10.1039/C4CC04479G.

15 Z. Li, R. Yu, J. Huang, Y. Shi, D. Zhang, X. Zhong, D. Wang, Y. Wu and Y. Li, Platinum–nickel frame within metal-organic framework fabricated in situ for hydrogen enrichment and molecular sieving, *Nat. Commun.*, 2015, **6**, 8248, DOI: 10.1038/ncomms9248.

16 L. Chen, X. Chen, H. Liu and Y. Li, Encapsulation of Mono- or Bimetal Nanoparticles Inside Metal–Organic Frameworks via In situ Incorporation of Metal Precursors, *Small*, 2015, **11**, 2642–2648, DOI: 10.1002/smll.201403599.

17 Y.-Z. Chen, R. Zhang, L. Jiao and H.-L. Jiang, Metal–organic framework-derived porous materials for catalysis, *Coord. Chem. Rev.*, 2018, **362**, 1–23, DOI: 10.1016/j.ccr.2018.02.008.

18 X. Liu, S. Zhang, S. Guo, B. Cai, S. A. Yang, F. Shan, M. Pumera and H. Zeng, Advances of 2D bismuth in energy sciences, *Chem. Soc. Rev.*, 2020, **49**, 263–285, DOI: 10.1039/C9CS00551J.

19 E. Zhang, T. Wang, K. Yu, J. Liu, W. Chen, A. Li, H. Rong, R. Lin, S. Ji, X. Zheng, Y. Wang, L. Zheng, C. Chen, D. Wang, J. Zhang and Y. Li, Bismuth Single Atoms Resulting from Transformation of Metal–Organic Frameworks and Their Use as Electrocatalysts for CO_2 Reduction, *J. Am. Chem. Soc.*, 2019, **141**, 16569–16573, DOI: 10.1021/jacs.9b08259.

20 Z. Zhang, M. Chi, G. M. Veith, P. Zhang, D. A. Lutterman, J. Rosenthal, S. H. Overbury, S. Dai and H. Zhu, Rational Design of Bi Nanoparticles for Efficient Electrochemical CO_2 Reduction: The Elucidation of Size and Surface Condition Effects, *ACS Catal.*, 2016, **6**, 6255–6264, DOI: 10.1021/acscatal.6b01297.

21 M. Miola, B. C. A. de Jong and P. P. Pescarmona, An efficient method to prepare supported bismuth nanoparticles as highly selective electrocatalyst for the conversion of CO2 into formate, *Chem. Commun.*, 2020, **56**, 14992–14995, DOI: 10.1039/D0CC06818G.

22 Y. Kong, X. Jiang, X. Li, J. Sun, Q. Hu, X. Chai, H. Yang and C. He, Boosting electrocatalytic CO2 reduction to formate via carbon nanofiber encapsulated bismuth nanoparticles with ultrahigh mass activity, *Chin. J. Catal.*, 2023, **45**, 95–106, DOI: 10.1016/S1872-2067(22)64177-9.

23 L.-B. Zhang, T. Tang, J. Fu, S. Niu, C. He, J.-S. Hu and L.-J. Wan, Molecular Linking Stabilizes Bi Nanoparticles for Efficient Electrochemical Carbon Dioxide Reduction, *J. Phys. Chem. C*, 2021, **125**, 12699–12706, DOI: 10.1021/acs.jpcc.1c03790.

24 X. Zhang, X. Sun, S.-X. Guo, A. M. Bond and J. Zhang, Formation of lattice-dislocated bismuth nanowires on copper foam for enhanced electrocatalytic CO2 reduction at low overpotential, *Energy Environ. Sci.*, 2019, **12**, 1334–1340, DOI: 10.1039/C9EE00018F.

25 Q. Gong, P. Ding, M. Xu, X. Zhu, M. Wang, J. Deng, Q. Ma, N. Han, Y. Zhu, J. Lu, Z. Feng, Y. Li, W. Zhou and Y. Li, Structural defects on converted bismuth oxide nanotubes enable highly active electrocatalysis of carbon dioxide reduction, *Nat. Commun.*, 2019, **10**, 2807, DOI: 10.1038/s41467-019-10819-4.

26 F. Yang, A. O. Elnabawy, R. Schimmenti, P. Song, J. Wang, Z. Peng, S. Yao, R. Deng, S. Song, Y. Lin, M. Mavrikakis and W. Xu, Bismuthene for highly efficient carbon dioxide electroreduction reaction, *Nat. Commun.*, 2020, **11**, 1088, DOI: 10.1038/s41467-020-14914-9.

27 X. Zhang, Y. Zhang, Q. Li, X. Zhou, Q. Li, J. Yi, Y. Liu and J. Zhang, Highly efficient and durable aqueous electrocatalytic reduction of CO2 to HCOOH with a novel bismuth–MOF: experimental and DFT studies, *J. Mater. Chem. A*, 2020, **8**, 9776–9787, DOI: 10.1039/D0TA00384K.

28 P. Lamagni, M. Miola, J. Catalano, M. S. Hvid, M. A. H. Mamakhel, M. Christensen, M. R. Madsen, H. S. Jeppesen, X.-M. Hu, K. Daasbjerg, T. Skrydstrup and N. Lock, Restructuring Metal–Organic Frameworks to Nanoscale Bismuth Electrocatalysts for Highly Active and Selective CO_2 Reduction to Formate, *Adv. Funct. Mater.*, 2020, **30**, 1910408, DOI: 10.1002/adfm.201910408.

29 J. Yang, X. Wang, Y. Qu, X. Wang, H. Huo, Q. Fan, J. Wang, L.-M. Yang and Y. Wu, Bi-Based Metal-Organic Framework Derived Leafy Bismuth Nanosheets for Carbon Dioxide Electroreduction, *Adv. Energy Mater.*, 2020, **10**, 2001709, DOI: 10.1002/aenm.202001709.

30 P. Deng, F. Yang, Z. Wang, S. Chen, Y. Zhou, S. Zaman and B. Y. Xia, Metal–Organic Framework-Derived Carbon Nanorods Encapsulating Bismuth Oxides for Rapid and Selective CO2 Electroreduction to Formate, *Angew. Chem., Int. Ed.*, 2020, **59**, 10807–10813, DOI: 10.1002/anie.202000657.

31 Y. Ying, B. Khezri, J. Kosina and M. Pumera, Reconstructed Bismuth-Based Metal–Organic Framework Nanofibers for Selective CO2-to-Formate Conversion: Morphology Engineering, *ChemSusChem*, 2021, **14**, 3402–3412, DOI: 10.1002/cssc.202101122.

32 L. Wu, Y. Luo, C. Wang, S. Wu, Y. Zheng, Z. Li, Z. Cui, Y. Liang, S. Zhu, J. Shen and X. Liu, Self-Driven Electron Transfer Biomimetic Enzymatic Catalysis of Bismuth-Doped PCN-222 MOF for Rapid Therapy of Bacteria-Infected Wounds, *ACS Nano*, 2023, **17**, 1448–1463, DOI: 10.1021/acsnano.2c10203.

33 K.-K. Yee, N. Reimer, J. Liu, S.-Y. Cheng, S.-M. Yiu, J. Weber, N. Stock and Z. Xu, Effective Mercury Sorption by Thiol-Laced Metal–Organic Frameworks: in Strong Acid and the Vapor Phase, *J. Am. Chem. Soc.*, 2013, **135**, 7795–7798, DOI: 10.1021/ja400212k.

34 H. Fei and S. M. Cohen, Metalation of a Thiocatechol-Functionalized Zr(IV)-Based Metal–Organic Framework for Selective C–H Functionalization, *J. Am. Chem. Soc.*, 2015, **137**, 2191–2194, DOI: 10.1021/ja5126885.

35 S. Pullen, H. Fei, A. Orthaber, S. M. Cohen and S. Ott, Enhanced Photochemical Hydrogen Production by a Molecular Diiron Catalyst Incorporated into a Metal–Organic Framework, *J. Am. Chem. Soc.*, 2013, **135**, 16997–17003, DOI: 10.1021/ja407176p.

36 B. Gui, K.-K. Yee, Y.-L. Wong, S.-M. Yiu, M. Zeller, C. Wang and Z. Xu, Tackling poison and leach: catalysis by dangling thiol–palladium functions within a porous metal–organic solid, *Chem. Commun.*, 2015, **51**, 6917–6920, DOI: 10.1039/C5CC00140D.

37 D.-C. Liu, T. Ouyang, R. Xiao, W.-J. Liu, D.-C. Zhong, Z. Xu and T.-B. Lu, Anchoring CoII Ions into a Thiol-Laced Metal–Organic Framework for Efficient Visible-Light-Driven Conversion of CO2 into CO, *ChemSusChem*, 2019, **12**, 2166–2170, DOI: 10.1002/cssc.201900338.

38 X.-L. Yang, J. Hu, H. Zhong, Q.-C. Lin, Z. Lin, L.-H. Chung and J. He, Building metal-thiolate sites and forming heterojunction in Hf- and Zr-based thiol-dense frameworks towards stable integrated photocatalyst for hydrogen evolution, *Chin. Chem. Lett.*, 2024, 110120, DOI: 10.1016/j.cclet.2024.110120.

39 M. Kandiah, M. H. Nilsen, S. Usseglio, S. Jakobsen, U. Olsbye, M. Tilset, C. Larabi, E. A. Quadrelli, F. Bonino and K. P. Lillerud, Synthesis and Stability of Tagged UiO-66 Zr-MOFs, *Chem. Mater.*, 2010, **22**, 6632–6640, DOI: 10.1021/cm102601v.

40 Y. Xin, Q. Gu, S. Cheng, D. H. Leng Seng, R. Ye, P. Borah and Z. Xu, Eu(III) Guests Sensitized by a Metal–Organic Framework for Sensing Cr(VI) in Strong Acids, *ACS Appl. Opt. Mater.*, 2024, **2**, 697–703, DOI: 10.1021/acsaom.4c00091.

41 X. He, Y. Guo, J. Zhang, S. Yang, J. Chen, S. Li, S. Xie, Y. Wang and C. Wang, Why can poorly conductive

Bi@UiO-MOF catalyze CO2 electroreduction?, *Chem. Commun.*, 2023, **59**, 5737–5740, DOI: 10.1039/D3CC00901G.

42 J. Toudert, R. Serna and M. Jiménez de Castro, Exploring the Optical Potential of Nano-Bismuth: Tunable Surface Plasmon Resonances in the Near Ultraviolet-to-Near Infrared Range, *J. Phys. Chem. C*, 2012, **116**, 20530–20539, DOI: 10.1021/jp3065882.

43 A. Cuadrado, J. Toudert and R. Serna, Polaritonic-to-Plasmonic Transition in Optically Resonant Bismuth Nanospheres for High-Contrast Switchable Ultraviolet Meta-Filters, *IEEE Photonics J.*, 2016, **8**, 1–11, DOI: 10.1109/JPHOT.2016.2574777.

44 D. Leng, T. Wang, Y. Li, Z. Huang, H. Wang, Y. Wan, X. Pei and J. Wang, Plasmonic Bismuth Nanoparticles: Thiolate Pyrolysis Synthesis, Size-Dependent LSPR Property, and Their Oxidation Behavior, *Inorg. Chem.*, 2021, **60**, 17258–17267, DOI: 10.1021/acs.inorgchem.1c02621.

45 S. Li, J. Chen, W. Jiang, Y. Liu, Y. Ge and J. Liu, Facile construction of flower-like bismuth oxybromide/bismuth oxide formate p-n heterojunctions with significantly enhanced photocatalytic performance under visible light, *J. Colloid Interface Sci.*, 2019, **548**, 12–19, DOI: 10.1016/j.jcis.2019.04.024.

46 P. P. Shanbogh, R. Raghunathan, D. Swain, M. Feygenson, J. Neuefeind, J. Plaisier, C. Narayana, A. Rao and N. G. Sundaram, Impact of Average, Local, and Electronic Structure on Visible Light Photocatalysis in Novel BiREWO6 (RE = Eu and Tb) Nanomaterials, *ACS Appl. Mater. Interfaces*, 2018, **10**, 35876–35887, DOI: 10.1021/acsami.8b08452.

47 H. Huang, X. Han, X. Li, S. Wang, P. K. Chu and Y. Zhang, Fabrication of Multiple Heterojunctions with Tunable Visible-Light-Active Photocatalytic Reactivity in BiOBr–BiOI Full-Range Composites Based on Microstructure Modulation and Band Structures, *ACS Appl. Mater. Interfaces*, 2015, **7**, 482–492, DOI: 10.1021/am5065409.

48 Y. Huang, S. Kang, Y. Yang, H. Qin, Z. Ni, S. Yang and X. Li, Facile synthesis of Bi/Bi2WO6 nanocomposite with enhanced photocatalytic activity under visible light, *Appl. Catal., B*, 2016, **196**, 89–99, DOI: 10.1016/j.apcatb.2016.05.022.

49 H. Liu, C. Du, M. Li, S. Zhang, H. Bai, L. Yang and S. Zhang, One-Pot Hydrothermal Synthesis of SnO2/BiOBr Heterojunction Photocatalysts for the Efficient Degradation of Organic Pollutants Under Visible Light, *ACS Appl. Mater. Interfaces*, 2018, **10**, 28686–28694, DOI: 10.1021/acsami.8b09617.

50 Y. Cheng, N. H. Shah, J. Yang, K. Zhang, Y. Cui and Y. Wang, Bi-Based Z-Scheme Nanomaterials for the Photocatalytic Degradation of Organic Dyes, *ACS Appl. Nano Mater.*, 2019, **2**, 6418–6427, DOI: 10.1021/acsanm.9b01373.

51 M. Kiani, S. Rizwan and S. Irfan, Facile synthesis of a BiFeO3/nitrogen-doped graphene nanocomposite system with enhanced photocatalytic activity, *J. Phys. Chem. Solids*, 2018, **121**, 8–16, DOI: 10.1016/j.jpcs.2018.05.014.

52 M. Suresh and A. Sivasamy, Bismuth oxide nanoparticles decorated Graphene layers for the degradation of Methylene blue dye under visible light irradiations and antimicrobial activities, *J. Environ. Chem. Eng.*, 2018, **6**, 3745–3756, DOI: 10.1016/j.jece.2017.01.049.

53 S. Subudhi, S. P. Tripathy and K. Parida, Metal oxide integrated metal organic frameworks (MO@MOF): rational design, fabrication strategy, characterization and emerging photocatalytic applications, *Inorg. Chem. Front.*, 2021, **8**, 1619–1636, DOI: 10.1039/D0QI01117G.

54 J. H. Cavka, S. Jakobsen, U. Olsbye, N. Guillou, C. Lamberti, S. Bordiga and K. P. Lillerud, A New Zirconium Inorganic Building Brick Forming Metal Organic Frameworks with Exceptional Stability, *J. Am. Chem. Soc.*, 2008, **130**, 13850–13851, DOI: 10.1021/ja8057953.

55 B. Guo, X. Cheng, Y. Tang, W. Guo, S. Deng, L. Wu and X. Fu, Dehydrated UiO-66(SH)2: The Zr–O Cluster and Its Photocatalytic Role Mimicking the Biological Nitrogen Fixation, *Angew. Chem., Int. Ed.*, 2022, **61**, e202117244, DOI: 10.1002/anie.202117244.

56 G. G. Briand, N. Burford and T. S. Cameron, The first ester complexes of bismuth(iii) using thiolate anchored bifunctional ligands, *Chem. Commun.*, 2000, 13–14, DOI: 10.1039/A907094J.

57 T. Ollevier, A. Jalba and H. Keipour, Bismuth(III) Nitrate Pentahydrate, in *Encyclopedia of Reagents for Organic Synthesis*, 2016, pp. 1–9.

58 C. Zou, S. Vagin, A. Kronast and B. Rieger, Template mediated and solvent-free route to a variety of UiO-66 metal–organic frameworks, *RSC Adv.*, 2016, **6**, 102968–102971, DOI: 10.1039/C6RA23947A.

59 A. Kumar Kar and R. Srivastava, Improving the Glucose to Fructose Isomerization via Epitaxial-Grafting of Niobium in UIO-66 Framework, *ChemCatChem*, 2022, **14**, e202200721, DOI: 10.1002/cctc.202200721.

60 N. Tsumori, L. Chen, Q. Wang, Q.-L. Zhu, M. Kitta and Q. Xu, Quasi-MOF: Exposing Inorganic Nodes to Guest Metal Nanoparticles for Drastically Enhanced Catalytic Activity, *Chem*, 2018, **4**, 845–856, DOI: 10.1016/j.chempr.2018.03.009.

61 T. Lu, Z. Du, J. Liu, H. Ma and J. Xu, Aerobic oxidation of primary aliphatic alcohols over bismuth oxide supported platinum catalysts in water, *Green Chem.*, 2013, **15**, 2215–2221, DOI: 10.1039/C3GC40730F.

62 Z. Wu, H. Wu, W. Cai, Z. Wen, B. Jia, L. Wang, W. Jin and T. Ma, Engineering Bismuth–Tin Interface in Bimetallic Aerogel with a 3D Porous Structure for Highly Selective Electrocatalytic CO2 Reduction to HCOOH, *Angew. Chem., Int. Ed.*, 2021, **60**, 12554–12559, DOI: 10.1002/anie.202102832.

63 C. D. Wagner and G. E. Muilenberg, *Handbook of X-ray photoelectron spectroscopy: a reference book of standard data for use in X-ray photoelectron spectroscopy*, by C.D. Wagner *et al.*, ed. G. E. Muilenberg, PerkinElmer Corp., Eden Prairie, Minn, 1979.

64 S. Daliran, A. R. Oveisi, C.-W. Kung, U. Sen, A. Dhakshinamoorthy, C.-H. Chuang, M. Khajeh, M. Erkartal and J. T. Hupp, Defect-enabling zirconium-based

metal–organic frameworks for energy and environmental remediation applications, *Chem. Soc. Rev.*, 2024, **53**, 6244–6294, DOI: 10.1039/D3CS01057K.

65 J. Ye, M. Neurock and D. G. Truhlar, Effect of Missing-Linker Defects on CO2 Hydrogenation to Methanol by Cu Nanoparticles in UiO-66, *J. Phys. Chem. C*, 2022, **126**, 13157–13167, DOI: 10.1021/acs.jpcc.2c03145.

66 D. A. Harrington and B. E. Conway, ac Impedance of faradaic reactions involving electrosorbed intermediates—I. Kinetic theory, *Electrochim. Acta*, 1987, **32**, 1703–1712, DOI: 10.1016/0013-4686(87)80005-1.

67 D. Lin and A. Lasia, Electrochemical impedance study of the kinetics of hydrogen evolution at a rough palladium electrode in acidic solution, *J. Electroanal. Chem.*, 2017, **785**, 190–195, DOI: 10.1016/j.jelechem.2016.12.037.

68 C. Y. J. Lim, M. Yilmaz, J. M. Arce-Ramos, A. D. Handoko, W. J. Teh, Y. Zheng, Z. H. J. Khoo, M. Lin, M. Isaacs, T. L. D. Tam, Y. Bai, C. K. Ng, B. S. Yeo, G. Sankar, I. P. Parkin, K. Hippalgaonkar, M. B. Sullivan, J. Zhang and Y.-F. Lim, Surface charge as activity descriptors for electrochemical CO_2 reduction to multi-carbon products on organic-functionalised Cu, *Nat. Commun.*, 2023, **14**, 335, DOI: 10.1038/s41467-023-35912-7.

69 Y. Huang, Y. Deng, A. D. Handoko, G. K. L. Goh and B. S. Yeo, Rational Design of Sulfur-Doped Copper Catalysts for the Selective Electroreduction of Carbon Dioxide to Formate, *ChemSusChem*, 2018, **11**, 320–326, DOI: 10.1002/cssc.201701314.

70 Y. Deng, Y. Huang, D. Ren, A. D. Handoko, Z. W. Seh, P. Hirunsit and B. S. Yeo, On the Role of Sulfur for the Selective Electrochemical Reduction of CO2 to Formate on CuSx Catalysts, *ACS Appl. Mater. Interfaces*, 2018, **10**, 28572–28581, DOI: 10.1021/acsami.8b08428.

71 P. Makuła, M. Pacia and W. Macyk, How To Correctly Determine the Band Gap Energy of Modified Semiconductor Photocatalysts Based on UV–Vis Spectra, *J. Phys. Chem. Lett.*, 2018, **9**, 6814–6817, DOI: 10.1021/acs.jpclett.8b02892.

72 X.-Q. Wu, J.-S. Shen, F. Zhao, Z.-D. Shao, L.-B. Zhong and Y.-M. Zheng, Flexible electrospun MWCNTs/Ag3PO4/PAN ternary composite fiber membranes with enhanced photocatalytic activity and stability under visible-light irradiation, *J. Mater. Sci.*, 2018, **53**, 10147–10159, DOI: 10.1007/s10853-018-2334-0.